Structure-Based Model of a Forced Shear Layer

K. Zhang*
Xi'an Jiaotong University, Xi'an 710049, China
and
A. M. Naguib[†] and M. M. Koochesfahani[†]
Michigan State University, East Lansing, Michigan 44824

The focus of this work is on assessing the ability of an array of discrete finite-core vortices to model vorticity-dominated flows where vortex sheets that have not fully rolled up into isolated vortices are present. The study extends our earlier work of modeling spatially periodic isolated vorticity in the wake of an oscillating airfoil. The present extension of the model is carried out by taking advantage of existing measurements in the unsteady flow of a forced two-stream shear layer. The shear-layer Reynolds number is 1.55×10^5, based on the velocity difference between the two streams and the streamwise location of the measurements. Single-component laser Doppler velocimetry is used to capture the transverse profiles of the streamwise velocity in the shear layer. Overall, the results show that the model provides good agreement with the experiments. The utility of the model is demonstrated by using it to establish possible physical connections between the flow features and the characteristics of the cross-stream profiles of the root-mean-square streamwise and transverse velocity. The model predictions are also found to exhibit small change with significant reduction in the number of vortex elements, highlighting the efficiency of the model and its potential usability in real-time flow control applications.

Nomenclature

c	=	airfoil chord
f	=	frequency, Hz
i, j	=	summation indices
k	=	reduced frequency
L_x	=	streamwise length of the vortex-array model
N	=	number of large-scale vortices in the vortex array model
n	=	number of small-scale vortices in the vortex array model
$R_{o,v}$	=	core radius of the large-scale vortices in the vortex-array model
$R_{o,vs}$	=	core radius of the small-scale vortices in the vortex-array model
r	=	ratio of low- to high-speed-stream streamwise velocity, U_2/U_1
$r_{i,v}$	=	radial coordinate measured from the center of the ith large-scale vortex in the vortex-array model
$r_{j,vs}$	=	radial coordinate measured from the center of the jth small-scale vortex in the vortex-array model
U	=	time-averaged streamwise velocity
U_o	=	average velocity of low- and high-speed streams
U_1	=	high-speed-stream velocity
U_2	=	low-speed-stream velocity
u	=	streamwise velocity
$\langle u \rangle$	=	phase-averaged streamwise velocity
u_{rms}	=	root mean square of the streamwise velocity
v	=	transverse velocity
v_{rms}	=	root mean square of the transverse velocity
X	=	streamwise coordinate

$X_{ci,v}$	=	streamwise coordinate of the core center of the ith large-scale vortex in the vortex-array model
$X_{cj,vs}$	=	streamwise coordinate of the core center of the jth small-scale vortex in the vortex-array model
X_m	=	streamwise coordinate of the measurements
Y	=	transverse coordinate
$Y_{ci,v}$	=	transverse coordinate of the core center of the ith large-scale vortex in the vortex-array model
$Y_{cj,vs}$	=	transverse coordinate of the core center of the jth small-scale vortex in the vortex-array model
Y_{max}	=	transverse coordinate of the maximum transverse gradient of the streamwise velocity
Y_o	=	transverse coordinate of the location where U is equal to U_o
α	=	angle of attack
a_o	=	angle of attack amplitude of oscillation
ΔU	=	difference between low- and high-speed stream velocities
Φ	=	oscillation cycle phase relative to the airfoil motion ($\Phi = 0$ corresponds to $\alpha = 0$ during pitch-up)
$\Gamma_{o,v}$	=	circulation of the large-scale vortices in the vortex-array model
$\Gamma_{o,vs}$	=	circulation of the small-scale vortices in the vortex-array model
λ	=	wavelength (corresponding to the streamwise spacing between successive large-sale vortices)
θ	=	momentum thickness of the shear layer
Ψ	=	oscillation cycle phase relative to the large-scale vortex ($\Psi = 0$ corresponds to vortex located at X_m)

I. Introduction

MUCH of modern fluid dynamics research has been aimed at understanding the flow structures dominating the transport properties of flows. One significant motivation for this type of research is to ultimately employ this understanding to construct structure-based (i.e., physics-based) models that can help with interpreting flow behavior in terms of the underlying organized motions and, *if possible*, with predicting certain flow characteristics. To date, however, there are very few examples of structure-based models. These include those of Perry and Chong [1], Perry et al. [2], and Ahn et al. [3] in turbulent wall-bounded flows, and Acton [4] and Kitaplioglu and Kibens [5] in jet flows. More recently, Naguib et al. [6] employed a simple, viscous-core-vortex-array model to compute

the unsteady velocity field in the wake of a periodically pitching airfoil embedded in a uniform flow. The model predictions agreed well with experimental data of the streamwise velocity in the wake of an oscillating NACA 0012 airfoil. The model was also successful in estimating the mean thrust acting on the airfoil.

Modeling of the wake in [6] is focused on the "far" wake, where the boundary layers separating from the trailing edge of the airfoil have completely rolled up into concentrated vortices. Thus, a question arises whether the idea of using an array of discrete finite-core vortices could also be extended to model flow situations where vortex sheets are present and the shed vorticity has not fully rolled up into detached isolated vortices (such as near the trailing edge of oscillating airfoils). Interest in extending the model to these situations stems from the fact that, because the model is based on the use of a relatively small number of discrete vortices with known analytical velocity field, the model is very simple to construct, efficient to run, and can represent vortex-dominated flow fields with good accuracy (as demonstrated in [6]). It is important to distinguish this type of low-order modeling from the more resource-intensive Lagrangian vortex particle methods (e.g., see the review by Leonard [7]), which are high-fidelity direct-numerical-simulation-like approaches. In particle methods, each vortex particle represents the vorticity at a point, rather than an entire vortex, or an extended spatial domain.

The present work takes advantage of an existing data set of a two-stream shear layer, forced by a periodically pitching airfoil placed at the center of the shear layer [8]. The main objective is to advance physics-based modeling using viscous-core-vortex arrays, rather than to understand the physics of the forced two-stream shear layer. The shear layer mainly serves as a testbed for assessing the modeling ideas; as such, applications of the model extend well beyond the plane two-stream shear layer. These applications include flapping-wing flight, bio propulsion, forced free and impinging jets, and more generally flows where organized vorticity forms from disturbed shear layers. It should also be added that the most important benefit of physics-based, low-order models, like the present one, is when they are used in conjunction with limited or comprehensive computational and/or experimental data to interpret observations of the velocity field in terms of the underlying flow features and their characteristics.

Other benefits include complementing single-point measurements and flow visualizations to extract flow structure information; understanding qualitative, or possibly even quantitative, variation in certain flow quantities with changes in the vortex characteristics; and developing data assimilation models. Recent demonstrations of some of these uses include [9], where a vortex array model is used to examine the connection between the parameters characterizing the wake vortex pattern of an oscillating airfoil and the mean airfoil thrust, and [10,11], where the model is employed to clarify hypotheses regarding the vortex behavior and the dynamics in the wake of oscillating tandem hydrofoils. In the current work, utility of the vortex-array model is exemplified by using the model to clarify connections between the flow structure of a two-stream shear layer and the characteristics of the experimentally observed fluctuating-velocity *rms* profiles across the shear layer.

II. Experiment

Details of the experimental data have been reported elsewhere [8]. Essential information is described here briefly for completeness. The experiment is conducted in a low-speed water tunnel. A two-dimensional shear-layer with a velocity ratio, $r = U_2/U_1 \approx 0.44$ is produced downstream of a splitter plate in the water tunnel. The flow velocity of the high-speed stream U_1 is 20.6 cm/s, resulting in Reynolds number based on $\Delta U = U_1 - U_2$, of about 1150/cm. A NACA 0012 airfoil with chord $c = 8$ cm and extending across the span of the water tunnel is pitched about the 1/4-chord point in the center of the shear layer, as depicted schematically in Fig. 1. The pitch axis of the airfoil is placed 27 cm downstream of the trailing edge of the splitter plate, and at a transverse location where the mean velocity equals the average of the low- and the high-speed stream velocities: $U_o = (U_1 + U_2)/2$. The chord Reynolds number based on U_o is approximately 12,000. The airfoil is pitched sinusoidaly with amplitude α_o of 4 deg around a mean angle of attack of zero at a frequency $f = 0.25$ Hz. The corresponding reduced frequency is $k = \pi f c/U_o = 0.42$. The angle of attack α of the airfoil is recorded simultaneously with the velocity using an RVDT to enable calculation of phase-averaged quantities relative to the airfoil motion (i.e., oscillating perturbations).

Measurement of the streamwise velocity is conducted using an Laser Doppler Velocimeter in the dual scatter mode at streamwise location $X = 135$ cm, where the Reynolds number based on X is 1.55×10^5, over a range $-0.15 < (Y - Y_o)/X < 0.15$ in the transverse direction, where Y_o is the Y coordinate of the position where the mean velocity is U_o. This corresponds to $-6.7 < (Y - Y_o)/\theta < 7.7$, where θ is the momentum thickness:

$$\theta = \int_{-\infty}^{Y_m} \left[\frac{U_1 - U(Y)}{U_1 - U_m} \right] \left[\frac{U(Y) - U_m}{U_1 - U_m} \right] dY \qquad (1)$$

In this expression, $U(Y)$ is the time-averaged (mean) streamwise velocity profile, U_m the minimum velocity in the profile, and Y_m the Y location where $U = U_m$. The momentum thickness will be used to
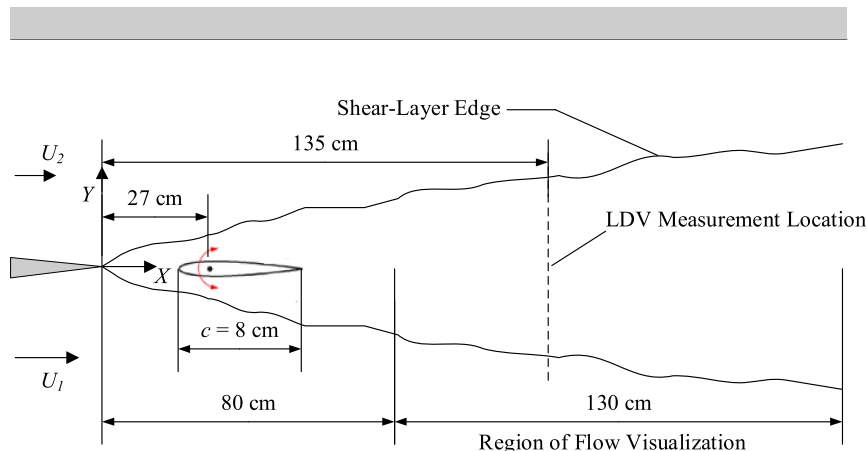

Fig. 1 Sketch of the experimental configuration and employed coordinate system (not to scale).

nondimensionalize all length scales in the remainder of the paper. For reference, the shear layer thickness is approximately 8θ (see Fig. 2, left), and the wavelength λ of the forced shear layer disturbance is $U_0/f\theta = \lambda/\theta = 17.8$.

III. Experimental Results

The flow visualization images in Fig. 3, taken from Koochesfahani and Dimotakis [8], show the change of the flow structures and the growth rate of the shear layer downstream of the airfoil when it is pitching periodically. As would be expected, organized vortex structures roll up in the wake of the oscillating airfoil as a result of forcing the shear layer. Figure 2 depicts the corresponding cross-stream profiles of the mean and the root means square (*rms*) streamwise velocity u_{rms}, where

$$U(Y) = \frac{1}{T} \int_0^T u(Y, t) \, dt \qquad (2)$$

$$u_{rms}(Y) = \sqrt{\frac{1}{T} \int_0^T \left(u(Y, t) - U(Y) \right)^2 dt} \qquad (3)$$

The mean velocity profiles for the natural and forced shear layers are very similar. However, the *rms* profiles are strikingly different in magnitude and shape. The latter change from a single-peaked profile, for the natural shear layer, to a triple-peaked distribution, in the presence of forcing.

Phase-averaged streamwise velocity ($\langle u \rangle$) profiles for the forced shear layer are shown in Fig. 4. To obtain these profiles, the oscillation cycle is subdivided into 50 equal, nonoverlapping intervals spanning from the beginning of the oscillation cycle (corresponding to airfoil angle of attack of 0 deg during the pitch-up phase), designated as $\Phi = 0$, to the end of the cycle, designated as $\Phi = 1$. The streamwise-velocity data are sorted into these intervals, or phase bins, based on the simultaneously recorded angle of attack information, and data falling into the same phase bin are averaged to get the phase-averaged velocity. Figure 4 displays the profiles at eight different phases of the oscillation cycle: $\Phi = 0$ to 0.875 in increments of 0.125. The red lines superposed on the profile correspond to boundaries of the "high-shear" region where the velocity gradient

$d\langle u \rangle/dY$ is within 50% of the maximum gradient magnitude at the same oscillation phase.

The velocity profiles in Fig. 4 show that the high-shear region is concentrated in a relatively narrow zone over a good portion of the oscillation cycle. This zone shifts progressively in the positive cross-stream direction with increasing time (as shown by the arrow on top of the figure) from below, at $\Phi = 0.75$, to above the shear-layer centerline. In the remainder of the oscillation cycle, the high-shear region widens to eventually encompass most of the measurement domain. An explanation of this behavior can be reached by inspection of the underlying flow structure, seen in the flow visualization picture in Fig. 4. The picture clearly depicts two vortical structures, forming from the roll-up of the shear layer in response to the airfoil oscillation. The two vortical structures, which are expected to produce a shear region spanning a domain of the same size as the vortex, are connected with a "braid" that is much smaller in cross-stream scale and is inclined at an angle relative to the streamwise direction. As the braid convects past the fixed X location of the measurements, one would expect it to produce a narrow zone of high shear that progressively moves in the upward direction with increasing time due to the inclination of the braid. As the upstream end of the braid travels past the measurement location, the measured shear zone is anticipated to gradually increase in cross-stream scale, eventually spanning the full shear-layer width, as the braid is followed by a large-scale vortex. These observations are consistent with the characteristics of the phase-averaged velocity profiles discussed above.

IV. Vortex-Array Model

A vortex-array model based on ideas similar to those employed in Naguib et al. [6] is used to represent the forced shear layer. The model is constructed by prescribing a streamwise-periodic spatial distribution of vorticity that is consistent with the flow features discussed in the previous section. Thus, one wavelength λ of the prescribed vorticity field is composed of one large-scale vortex (LV) and a number of smaller vortices representing the braid, or "vortex sheet" (VS), which "connects" the LVs, as illustrated in Fig. 5. All vortices are assumed to have a core with Gaussian vorticity distribution with the circulation of the vortices representing the VS given by $\Gamma_{o,vs}$, and that of the LV is $\Gamma_{o,v}$. The corresponding core radii are $R_{o,vs}$ and $R_{o,v}$, respectively, with the latter expected to be larger than the former. It should be noted that the use of the flow features
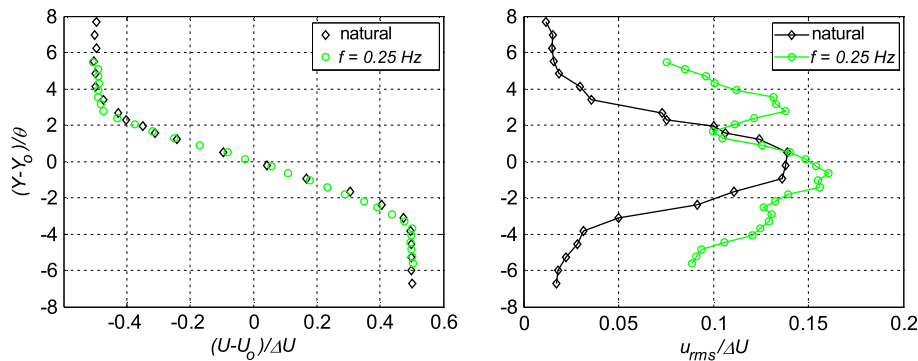

Fig. 2   Mean (left) and *rms* (right) streamwise-velocity profiles at $X = 135$ cm.

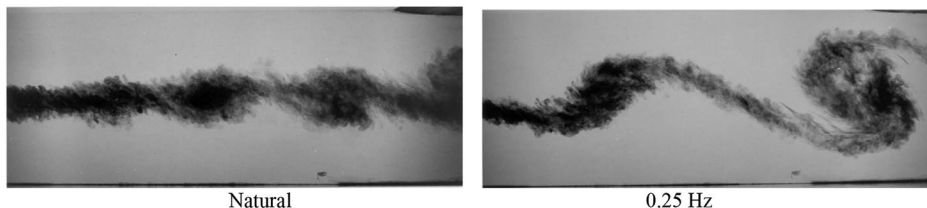| Natural | 0.25 Hz |

Fig. 3   Dye flow visualization from Koochesfahani and Dimotakis [8] showing the shear-layer vortical structures downstream of the airfoil for the natural (left) and forced (right) shear layer.
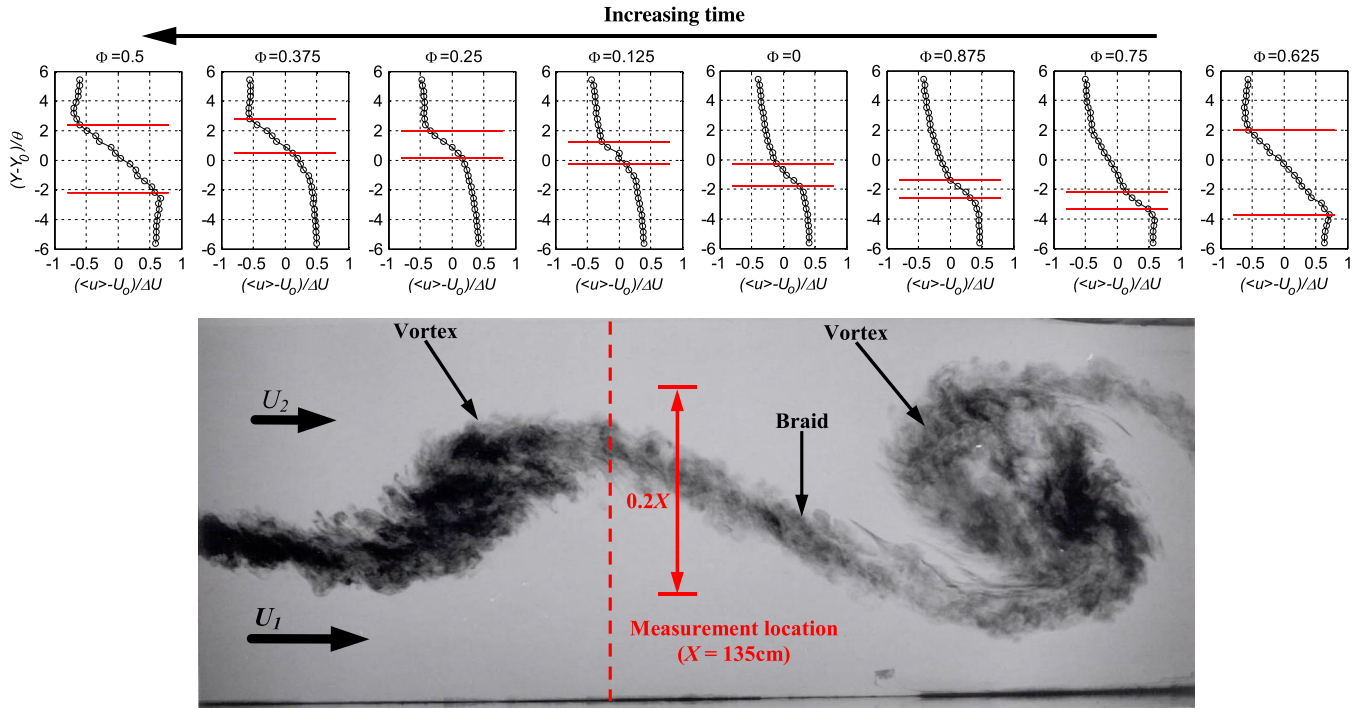
Fig. 4 Streamwise-velocity profiles obtained from an average at selected phases of the oscillation cycle for the forced shear layer (top), and flow visualization image depicting the corresponding flow structure (bottom). The phase closest to the visualization instance is Φ = 0.25.
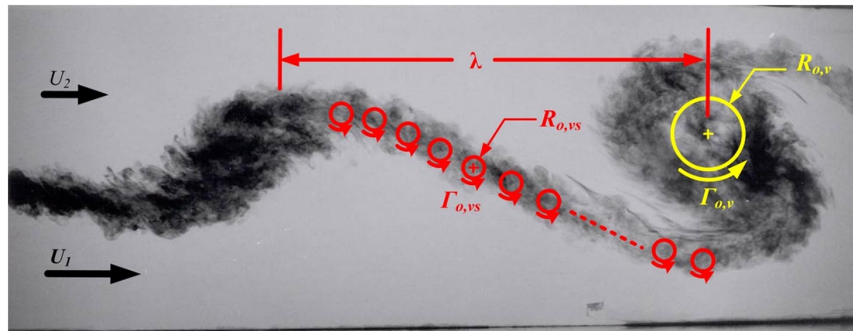

Fig. 5 Illustration of the arrangement of the Gaussian-core vortices used to model the braid (red) and large-scale vortex (yellow) over one wavelength λ.

inferred from the flow visualization as the basis for modeling the vorticity distribution may be misleading [12], because the evolution of the dye features is dependent on the scalar diffusivity, whereas the development of the vorticity field is tied to the kinematic viscosity. These two quantities are only identical for a flow situation with a unity Schmidt number. For dye, the Schmidt number is of order 1000. However, even for such a large discrepancy in the scalar and viscous diffusivity, the dye captures the vortical features well, provided that the dye is injected at the location of vorticity generation and that the visualization location is close to the place of introduction of the dye [13]. Ultimately, the appropriateness of the vortex array model is gaged by the success of the model's reproduction of the experimental velocity data. From a more general perspective, the model enables the attainment of quantitative information of the velocity field based on qualitative interpretations from flow visualization of vorticity dominated flows. Comparison of these calculations with limited experimental information facilitates verification of the flow visualization interpretations. As such, *together*, flow visualization and the finite-core-vortex array model could provide an efficient and robust tool for identification of vortical flow features in a wide range of flows.

The final vorticity distribution of the model is obtained by repeating the vortex-array configuration shown in Fig. 5 N times in the streamwise direction with a wavelength $\lambda = U_o/f$ to mimic the periodic shear-layer vortex structure. Unlike the actual flow,

however, where the circulation and scale of the LVs and the braid characteristics change in the streamwise direction, the characteristics of the vortex array shown in Fig. 5 are selected to match the vorticity characteristics at the measurement location, but then kept unchanged when periodically extending the array. This is done for simplicity and with the expectation that variation in the vorticity distribution within wavelengths other than the one containing the calculation location will cause minimal difference in the computed velocity. Specifically, the *induced* velocity is calculated from the prescribed vorticity distribution using the Biot-Savart law. Based on the latter, it can be shown that the difference between the actual and frozen vorticity distribution within wavelengths other than that containing the calculation location relate to the dipole and higher-order poles of the vortex pattern in these distant wavelengths. The corresponding induced velocity decays at least quadratically with distance, and hence these differences should have minimal, if any, influence on the computed velocity. The negligible influence of higher-order moments on the induced velocity is also discussed in reference [14] for the specific case of a two-stream shear layer.

Using the Biot-Savart law, it can be shown that the streamwise (u) and the transverse (v) components of the velocity induced at a point (X, Y) by the vortex array, including N large vortices (which is also equal to the number of wavelengths λ included in the model) and $n \times N$ small vortices, superposed onto a uniform flow with streamwise velocity U_o are given by

$$u(X, Y) = U_0 - \sum_{i=1}^{N} \frac{\Gamma_{i,v}(r_{i,v})}{2\pi} \frac{(Y - Y_{ci,v})}{r_{i,v}^2}$$

$$- \sum_{j=1}^{nN} \frac{\Gamma_{j,vs}(r_{j,vs})}{2\pi} \frac{(Y - Y_{cj,vs})}{r_{j,vs}^2} \qquad (4)$$

$$v(X, Y) = \sum_{i=1}^{N} \frac{\Gamma_{i,v}(r_{i,v})}{2\pi} \frac{(X - X_{ci,v})}{r_{i,v}^2} + \sum_{j=1}^{nN} \frac{\Gamma_{j,vs}(r_{j,vs})}{2\pi} \frac{(X - X_{cj,vs})}{r_{j,vs}^2} \qquad (5)$$

with

$$\Gamma_{i,v}(r_{i,v}) = \Gamma_{o,v}[1 - e^{-(r_{i,v}/R_{o,v})^2}] \qquad (6)$$

$$\Gamma_{j,vs}(r_{j,vs}) = \Gamma_{o,vs}[1 - e^{-(r_{j,vs}/R_{o,vs})^2}] \qquad (7)$$

where $(X_{ci,v}, Y_{ci,v})$ is the coordinate of the center of the ith LV, $(X_{cj,vs}, Y_{cj,vs})$ is the coordinate of the center of the jth small vortex along the VS, and $r_{i,v}$ and $r_{j,vs}$ are the radial coordinates measured from the center of the ith LV and the jth small vortex, respectively, to point (X, Y). Equations (4–7) yield the velocity field at a given instant in time. For a given X location, the time-dependent velocity field is obtained by advecting the streamwise coordinates $X_{ci,v}$ and $X_{cj,vs}$ in the streamwise direction at a velocity given by λf. This way of evolving the flow field, which is based on Taylor's frozen field hypothesis, is a gross simplification, yet it appears to represent the flow reasonably well, as will be seen below. More generally, the velocity field may be evolved in time taking into account the mutual interaction of the vortical features via the Bio-Savart law. Based on the results given below, this is not expected to provide significant quantitative difference from the results shown here for a given X location. However, accounting for the mutual interaction of vortical features should provide an overall more realistic *streamwise evolution* of the flow as well as better quantitative results over an *extended* streamwise domain.

To determine the model parameters for a given case, a three-step approach is used:

1. *Preliminary* estimation of the LV parameters $\Gamma_{o,v}$ and $R_{o,v}$ by minimizing the difference between the calculations of the model without the VS (i.e., $n = 0$) and the measured velocity profile at the cycle phase when the LV is present at the measurement location.

2. Computation of a *residual* phase-resolved velocity profile by subtracting the velocity computed using the LV-only model from step 1 from the overall experimental phase-resolved velocity profile. The residual profile, which predominantly captures the velocity due to the VS alone, facilitates determination of the VS locus along which the small-vortex centers $(X_{cj,vs}, Y_{cj,vs})$ are deployed.

3. Optimization of the complete set of parameters of the full model, including further refinement of the parameters determined in step 1.

Details of each of the above three steps may be found in Appendix A.

The number of small vortices n in each wavelength and the number of large vortices N (or the streamwise length of the model $L_x = N\lambda$) in the model are set based on the convergence of the velocity calculation, that is, when the calculation does not change with the addition of more vortices to the model. Figure 6 depicts the model computation of the mean streamwise velocity $(U - U_0)/\Delta U$, the *rms* streamwise velocity $u_{rms}/\Delta U$, and the *rms* transverse velocity $v_{rms}/\Delta U$ for different n values while keeping $L_x/\lambda = N = 100$ (except for the solid black line where $N = 10$). Figure 7 shows the same quantities but for different number of wavelengths while keeping $n = 200$ (except for the solid black line where $n = 20$): $L_x/\lambda = N = 10, 20, 50,$ and 100 (the values for other model parameters are given in Table 1). As seen in Figs. 6 and 7, it is difficult to discern the difference between the computed profiles without the high-magnification inset provided in the plot when $n \geq 100$ and $L_x/\lambda = N \geq 50$. The model requires a relatively large number of vortices to converge (more than approximately 5000), but it only requires a few minutes to run when implemented in MATLAB
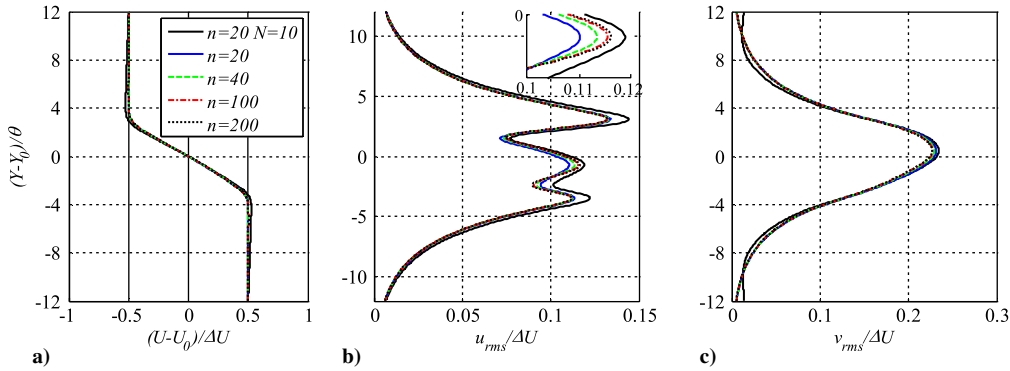
Fig. 6 Dependence of the computed velocity profiles on n with $L_x/\lambda = N = 100$ (except for the solid black line for which $N = 10$): a) mean streamwise velocity; b) *rms* streamwise velocity; c) *rms* transverse velocity. Inset in (b) provides a magnified view of the middle peak in the plot.
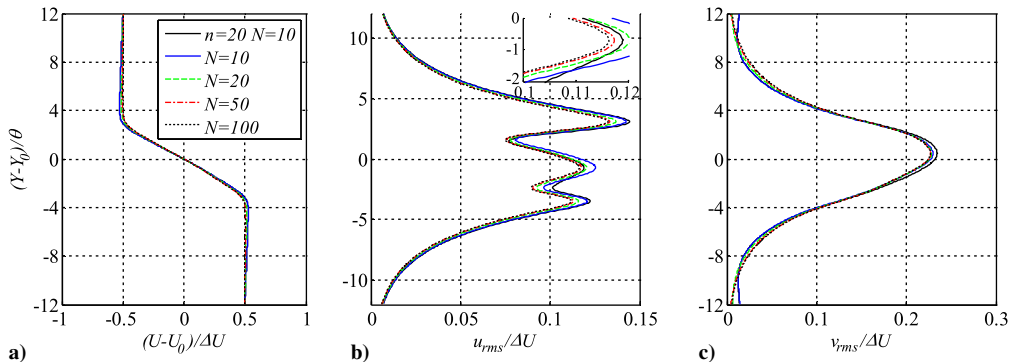
Fig. 7 Dependence of the computed velocity profiles on N with $n = 200$ (except for the solid black line for which $n = 20$): a) mean streamwise velocity; b) *rms* streamwise velocity; c) *rms* transverse velocity. Inset in (b) provides a magnified view of the middle peak in the plot.

Table 1   Values of the parameters of the vortex-array model

$\Gamma_{o,v}/\Delta U\theta$	$R_{o,v}/\theta$	$\Gamma_{o,vs}/\Delta U\theta$	$R_{o,vs}/\theta$	dYc/θ	n	$L_x/\lambda = N$
8.03	2.09	0.044	0.79	0.135	200	50

on a PC. For all subsequent calculations reported here, $n = 200$ and $L_x/\lambda = N = 50$. The vorticity field obtained from the resulting vortex-array model is shown in Fig. 8. It is noteworthy, however, that using the model with a much smaller number of vortices (200, with $n = 20$ and $N = 10$), the resulting mean and *rms* velocity profiles are not significantly different from those of the converged model (compare the solid and the broken black lines in Figs. 6 and 7). This implies that at the expense of a relatively small difference, the model could be much more efficient to run, making it potentially useful for real-time flow control applications.

V.   Results

In this section, the model calculations, using the optimized parameters (given in Table 1), are compared with the experimental data. In Table 1, dY_c is a parameter representing the cross-stream offset of the LV core center. Also, it is interesting to consider the total circulation of the shear layer per unit wavelength; that is, $\Gamma/\lambda = \Gamma_{o,v}/\lambda + n\Gamma_{o,vs}/\lambda$. Based on the circulation values in Table 1, and $\lambda/\theta = 17.8$, $\Gamma/\lambda = 0.95\Delta U$, which is consistent with $\Gamma/\lambda \sim 1$ for shear layers (e.g., see [14]). Figure 9 displays a comparison between the computed and the measured streamwise velocity profiles at 10 different phases of the oscillation cycle ($\Psi = 0$ to 1 in

steps of 0.1). Note that Ψ is shifted by 0.55 relative to Φ (the oscillation cycle phase used hitherto) such that $\Psi = 0$ corresponds to the center of the core of the large-scale vortex coinciding with the calculation location (see Fig. 8 for connecting Ψ values to the streamwise location along the shear layer).

Overall, Fig. 9 shows that the model results agree remarkably well with the experimental data at most phases in the oscillation cycle, specially between $\Psi = 0.2$ and 0.7, when the central part of the VS passes through X_m. This indicates that this part of the VS is modeled properly. However, some subtle differences can be seen, particularly at phases between $\Psi = 0$ and 0.1 and $\Psi = 0.8$ and 0.9 when the LV is close to X_m. For example, the computed velocity overestimates the measured values for $-1 < (Y - Y_o)/\theta < 6$ at $\Psi = 0.1$, and the computed velocity is lower than the measured values below Y_o at $\Psi = 0.9$. It is suspected that further refinement of the detailed structure of the VS may remedy these subtle differences. Such refinements may include a nonlinear description of the VS shape, particularly where it connects with the LV, and allowing the small-vortex properties ($\Gamma_{o,vs}$ and $R_{o,vs}$) to vary along the vortex sheet. These modifications, however, would add complexity that is likely unnecessary given that the difference between the model computations and the measurements is rather small.

Additional comparison between the computed and measured velocity is given in Fig. 10 for the mean and *rms* velocity profiles. No experimental data are shown for v_{rms} (Fig. 10c), because only the streamwise component of the velocity was measured. The v_{rms} results are shown for reference and to highlight an advantage of the model in augmenting limited experimental data with additional information. Also, the symbols in Figs. 10a and 10b represent mean and *rms*
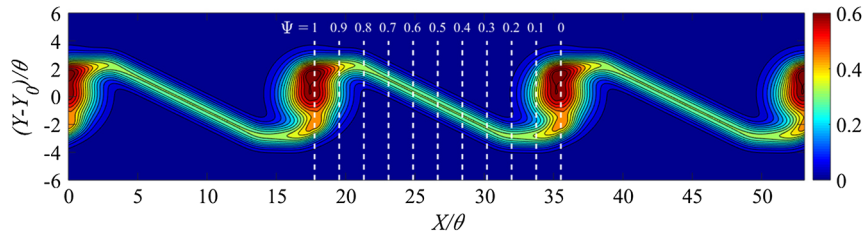
Fig. 8   Contour plot of the nondimensional vorticity field $\omega_z\theta/\Delta U$ obtained from the vortex-array model. The broken white lines identify the locations corresponding to the phases at which streamwise velocity profiles are plotted in Fig. 9. Model parameters are listed in Table 1. $X = 0$ is set arbitrarily.
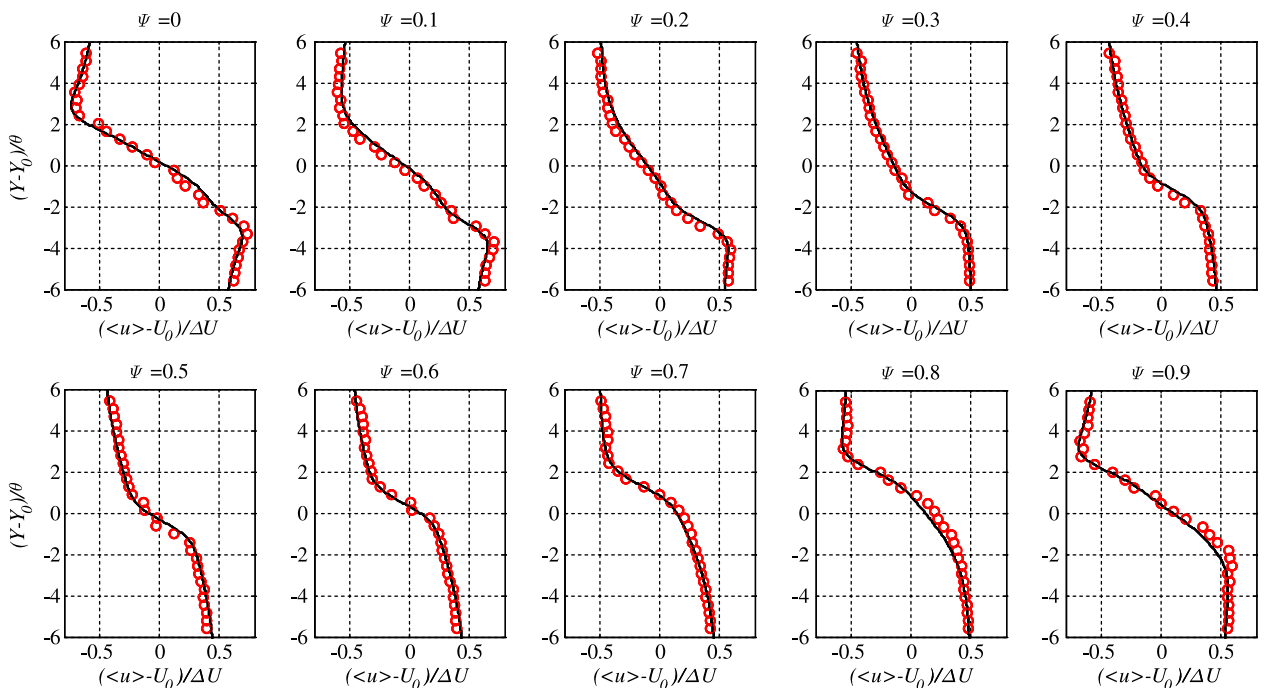
Fig. 9   Comparison of the computed (line) and measured (symbols) streamwise velocity profiles at selected phases of the oscillation cycle. The locations of the shear layer corresponding to the phases shown are identified with white broken lines in Fig. 8.
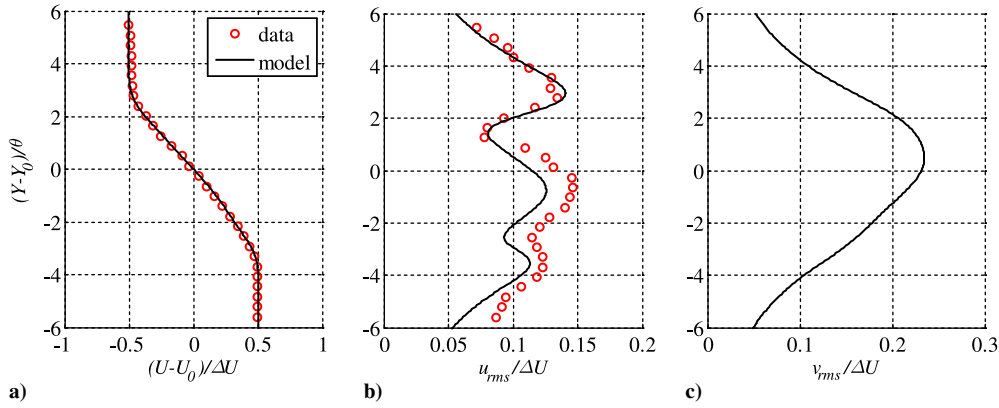
Fig. 10   Comparison of the computed (line) and measured (symbols) velocity profiles: a) mean streamwise velocity; b) *rms* streamwise velocity; and c) rms transverse velocity.

streamwise velocity profiles calculated from the phase-averaged experimental data of 20 selected phases of the oscillation cycle ($\Psi = 0$ to 0.95 in steps of 0.05), rather than from the long time series. Thus, the *rms* profiles differ from those presented in Fig. 2 in that any random velocity fluctuations that are not phase-locked to the airfoil motion (e.g., due to cycle-to-cycle variation in the cross-stream location of the LV core center) are not captured in the data shown in Fig. 10. As seen from Fig. 10, the model gives good reproduction of the mean streamwise velocity. Additionally, the computed *rms* streamwise velocity is in excellent qualitative agreement with the experimental data, depicting a triple-peaked u_{rms} profile shape; though the overall magnitude is under estimated for $(Y - Y_0)/\theta < 1$.

The main advantage of the vortex-array model is when used as a tool for understanding of the flow physics. To demonstrate, we examine how the observed features of the *rms* profiles relate to the characteristics of the flow structures. To this end, the contribution of the VS or the LV to the computed velocity is "turned off" in order to understand the induced velocity characteristics of each one of these two features by itself. Figure 11 depicts contour plots of the computed phase-resolved velocity of the LV alone (Fig. 11a), the VS by itself (Fig. 11b), and the two combined (i.e., obtained from the full model; Fig. 11c). In each case, the mean velocity $U(Y)$ is subtracted to emphasize the unsteady flow features. As would be expected, when considering the large-scale vortex only, the largest induced velocity magnitude occurs at the phase when the vortex is at the calculation location ($\psi = 0$; or 1) and at Y locations of approximately $\pm R_{o,v}$ away from the vortex center. In contrast, at the Y location of the vortex center, near $(Y - Y_0)/\theta = 0$, there is no variation in velocity with phase (as implied from the horizontal orientation of the velocity contours). Thus, on its own, the LV is expected to produce the strongest streamwise velocity variation at Y locations that are approximately $\pm R_{o,v}$ away from vortex core center, and no variation at the location of the center: a known feature of Gaussian vortices.

On the other hand, when considering the VS alone (Fig. 11b), the corresponding contour plot clearly captures the sheet, depicted as a narrow zone of densely packed contour lines that stretch over the full cycle. Consistent with the modeled locus of the vortex sheet (Fig. 15, right), this zone has two "horizontal" parts ("head" and "tail") that approximately span the first and last 30% of the cycle. These are the

VS parts that reside on top and bottom of, and are getting entrained into the LV. The remainder of the VS is made up of an inclined shear layer. Referring to Fig. 11b, it is evident that the inclined part of the VS is associated with the largest velocity change with phase and that this change is fairly uniform with Y. This velocity variation is associated with the change in u produced by the shear across the sheet as the sheet advects past the observation location. The head and tail of the vortex sheet do not produce similar variation because the associated shear is orthogonal to the advection direction. However, these parts produce localized velocity fluctuation peaks that are collocated in phase with the head and tail but reside at Y locations that are above and below the head and tail, respectively. These velocity variations are related to the *finite length* of the "horizontal" head and tail. In other words, a streamwise advecting horizontal vortex sheet that is infinitely long would produce no fluctuating velocity because, as stated earlier, the advection does not result in movement of the shear past the velocity observation point. However, with a short-length VS, at any instant, the induced streamwise velocity of this layer varies with X, which would produce temporal variation in u when observing the velocity at a fixed point in space past that the VS advects.

The superposition of the phase-resolved velocity fluctuation in Figs. 11a and 11b produces the *full*-fluctuating-velocity contours in Fig. 11c. Although the resulting contour pattern is complex, the largest fluctuations seem to be centered around three Y locations: in the vicinity of the shear layer center, and outboard at $(Y - Y_o)/\theta \approx -3.5$ and 3 (as marked using horizontal broken lines in Fig. 11). Near the shear-layer centerline, the superposition of the velocity signatures of the LV and the VS produces a contour pattern that is similar to that produced by the inclined part of the VS alone (Fig. 11b) while being more localized (rather than spread/uniform). On the other hand, at the outboard locations, the phase difference between the fluctuating velocities of the LV and the VS (as seen from Figs. 11a and 11b) is such that a net constructive superposition takes place at $(Y - Y_o)/\theta \approx -3.5$ and 3, producing large velocity fluctuation. Notably, the fluctuation velocity is not as large at $(Y - Y_o)/\theta \approx \pm R_{o,v}/\theta \approx \pm 2$ as was the case in Fig. 11a for the LV alone. This is because, at these locations, the superposition of the vortex and the braid influences does not produce fluctuation as strong as found at $(Y - Y_o)/\theta \approx -3.5$ and 3. In other
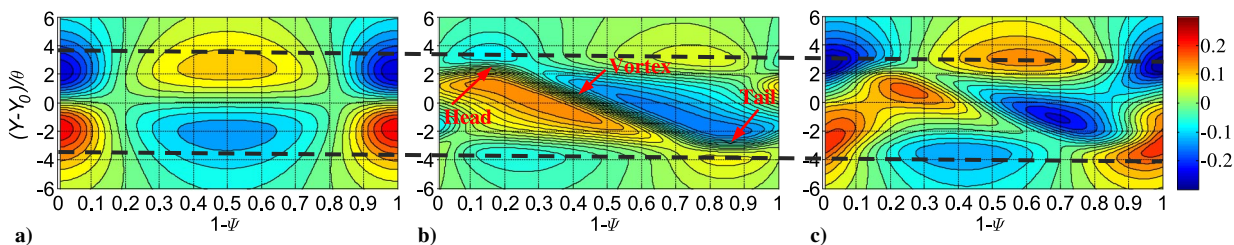
Fig. 11   Computed *mean-removed* phase-resolved velocity $[\langle u \rangle - U(Y)]/\Delta U$ due to the LV (a), the VS (b), and their combination (c). The horizontal broken lines are used to identify the Y locations of the outboard u_{rms} peaks from Fig. 10b.
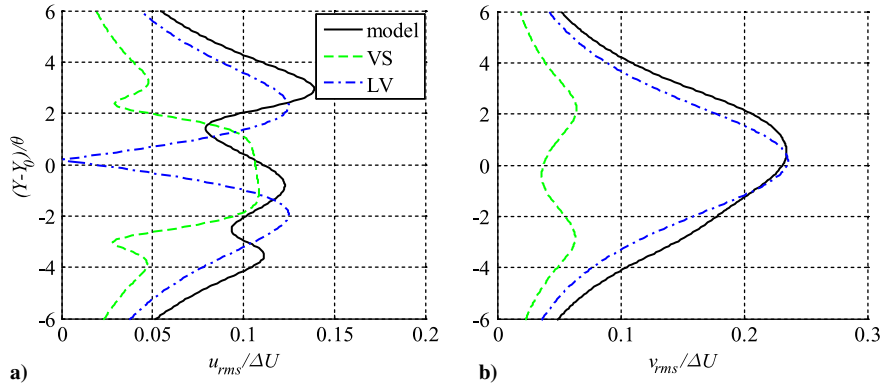
Fig. 12   Velocity profiles induced by the vortex sheet and large-scale vortex: a) *rms* streamwise velocity; b) *rms* transverse velocity.

words, the presence of the vortex sheet shifts the outboard locations of the largest fluctuations away from those corresponding to the LV by itself: $(Y - Y_o)/\theta \approx \pm R_{o,v}/\theta$.

The conclusions of Fig. 11 are further reinforced using Fig. 12, where the u_{rms} profile in Fig. 10b, obtained from the model, is reproduced in Fig. 12a and compared with the u_{rms} profiles due to the LV and the VS. The profile associated with the LV exhibits the expected two peaks that are located approximately one core radius away from the vortex center with zero u_{rms} at the center. On the other hand, the vortex sheet profile possesses a shape that is commensurate with the analysis of Fig. 11b. Specifically, the profile has a fairly uniform central part near the middle of the shear layer, which is the result of the advection of the inclined part of the VS. Two local minima coincide with the location of the head and tail, with two nearby local maxima associated with the induced velocity by these parts. The three peaks of the overall u_{rms} are thus predominantly produced by the inclined VS (the middle peak), and the LV together with the induced velocity by the head and tail of the VS (the two outboard peaks). It is interesting to note that though the LV contribution to these outboard peaks is generally larger than the contribution of the head and tail, the actual peak locations coincide with the outboard peaks of the u_{rms} of the vortex sheet (for the reasons given in the discussion of Fig. 11c). Overall, it is reasonable to expect the relative prominence of the center versus the outboard peaks of the u_{rms} distribution to depend on the development stage of the vortex. Early in the development stage, most of the vorticity is in the vortex sheet and hence one would expect the central peak to be more prominent relative to the outboard peaks. In comparison, when the vortex is fully formed, and hence the vortex sheet is weak or nonexistent, the u_{rms} profile would be dominated by the outboard peaks.

Figure 12b shows the full v_{rms} profile that exhibits a single maximum near the shear-layer center. Comparison with v_{rms} of the LV and the VS clearly shows the dominant influence of the LV on this component of the velocity. The VS v_{rms} profile possesses two local maxima at the locations of the head and tail. This is expected given that the velocity induced by the sheet normal to the sheet's centerline (which is in the Y direction in this case) is largest along the sheet's centerline. This is also true for the LV that exhibits a peak at the Y location where the vortex core center is located. The presence of the head and tail of the braid slightly enhances the v fluctuation produced by the large-scale vortex away from the shear-layer centerline, while they have no effect in the vicinity of the centerline.

In summary, the present work extends the capability of the vortex-array model of [6] to handle regions where separated shear layers have not completely rolled into detached vortices. It is important to note that the model's key advantage is not as a predictive tool, but rather as an instrument to understand the physics of flows by complementing computational and/or experimental information. The above analysis demonstrates the utility of the model (and other physics-based models in general) in probing flow physics in ways that are difficult to undertake using high-fidelity computational and experimental data alone, which are more suited for obtaining accurate flow quantities and phenomenological characterization of the flow

behavior. To be specific, we note that, for example, the present model allowed decomposition of the vortex sheet and the large-vortex influences on the streamwise velocity fluctuation, clarifying (among others) 1) the flow physics leading to the triple-peaked shape of the u_{rms} profile and 2) that the cross-stream locations of the side peaks in the u_{rms} distribution are not coincident with the core radius of the LV, as one might typically assume. Though these findings might have been hypothesized based on actual data, demonstrating their plausibility beyond hand waving would be very difficult without the benefit of a low-order model like the present one.

VI.   Conclusions

In this paper, it is found that an array of finite-core vortices is effective in modeling vortical flow regions where the vorticity distribution includes both vortex sheets and isolated vortices. This conclusion is reached by assessing the model using existing data of the unsteady streamwise velocity of a forced two-stream shear layer. Overall, the model results agree well with the experimental data at different phases of the oscillation cycle.

The utility of the model in understanding the physics of the underlying flow is exemplified by using the model to conduct an analysis to investigate the specific effect of different flow structures on the velocity field. The analysis shows that both the large-scale vortices and the braids influence the fluctuating streamwise velocity (u_{rms}) profiles. Two u_{rms} peaks, above and below the shear-layer centerline, are predominantly affected by the large-scale vortices. However, these peaks are also influenced by parts of the braid that are getting entrained into the vortex, at the top and bottom of the vortex, causing the cross-stream location of the u_{rms} peaks to deviate from those that would exist under the effect of the vortex alone. Additionally, the braid is found to be responsible for the generation of streamwise velocity fluctuations in the vicinity of the shear-layer centerline. Overall, the relative importance of the large vortices and the braids in producing streamwise velocity fluctuations appears to depend on the "completeness" of the shear-layer roll-up into a vortex (i.e., the stage of development of the vortex).

The model is used to obtain the fluctuating transverse velocity (v_{rms}) profile. Analysis of the latter shows that v_{rms} is mostly influenced by the large-scale vortex, which produces a v_{rms} profile with a maximum near the center of the shear layer. The maximum v_{rms} is found to be approximately twice that of u_{rms}. The v_{rms} information are predicted by the model because the experimental data are limited to the streamwise velocity only. These observations highlight the utility of the model in complementing limited data sets, in addition to enabling deeper insights into the underlying flow physics. The model also produces reasonable results with significant reduction in the number of vortex elements, demonstrating the model's potential utility for fast real-time calculations in flow control applications.

Appendix: Determination of Model Parameters

As described in Sec. IV, a three-step procedure is used to determine the vortex-array model parameters. In step 1, a simplified version of the model is created by considering the LV to be the only flow

structure; that is, by only using the first and second terms on the right-hand side of Eq. (4). The model parameters $\Gamma_{o,v}$ and $R_{o,v}$ are set by seeking the best match between the model calculation and the measurement of u at the phase when the large-scale vortex passes the measurement location. The "best match" is judged quantitatively when the sum of the squared error ε_Y^2 between the computed and measured velocity profile over all Y measurement locations reaches a minimum value. Specifically, the expression for ε_Y^2 is given by

$$\varepsilon_Y^2(\Phi) = \sum_Y \Big[\langle u(Y, \Phi)\rangle_c - \langle u(Y, \Phi)\rangle_m \Big]^2 \qquad (A1)$$

where $\langle u(Y, \Phi)\rangle_c$ is the computed velocity at location Y and the selected phase Φ, and $\langle u(Y, \Phi)\rangle_m$ the corresponding measured phase-averaged velocity.

The number of large vortices N in the model (or the streamwise length of the model $L_x = N\lambda$) is set based on the convergence of the

velocity calculation (see Figs. 6 and 7). Here $L_x/\lambda = N$ is set to 50. The phase of an LV passing through the measurement location is determined as that where the extent of the high-shear zone in the Y direction (as defined in Fig. 4) reaches a maximum value. This criterion avoids selecting a location where the VS is present at the measurement location because the scale of the vortex shear zone in the Y direction is appreciably larger than that of the vortex sheet (e.g., compare the shear zone extent at $\Phi = 0.625$ to that at $\Phi = 0$ in Fig. 4). However, it is found that the variation in the width of the shear zone varies slowly with phase in the vicinity of the phase where the shear zone extent is largest. Therefore, to "pin-point" the phase at which the vortex is collocated with the measurement location, the target phase is identified as that where the difference between the maximum and the minimum streamwise velocity is largest. The latter criterion is based on the fact that the largest streamwise velocity induced by the vortex occurs above and below the vortex core center.

Figure A1 shows the experimental data at the phase $\Phi = 0.55$ when the LV is determined to be at the measurement location. The data are compared with the calculation of the LV-only model using $\Gamma_{o,v}$ and $R_{o,v}$ values that minimize ε_Y in Eq. (A1). Overall, the two profiles are qualitatively consistent, though some qualitative differences are evident—notably the over- and undershoot at the peak and valley of the profile.

In step 2, residual streamwise-velocity profiles are obtained after subtracting the computed velocity induced by the LV from the measured data. The resulting profiles at different phases of the oscillation cycle are shown in Fig. A2. The diamond symbol in a given plot represents the location Y_{max} of the negative shear with maximum magnitude at a given phase of the oscillation cycle. This location is expected to be the center of the vortex sheet passing through the measurement location at the corresponding phase of oscillation. Notably, between $\Phi = 0.5$ and $\Phi = 0.6$, there are two local maxima in the magnitude of the negative shear on the upper and lower side of the shear-layer centerline.

Fig. 15 (left) shows Y_{max} versus phase using circles, which is seen to move in the positive Y direction (notwithstanding some data scatter) before dropping, fairly abruptly, at $\Phi = 0.55$, and then rising up again starting at $\Phi = 0.6$. The quick drop of Y_{max} from the highest to the lowest value should correspond to the passage of the LV past X_m around $\Phi = 0.55$, and the accompanying change in the VS
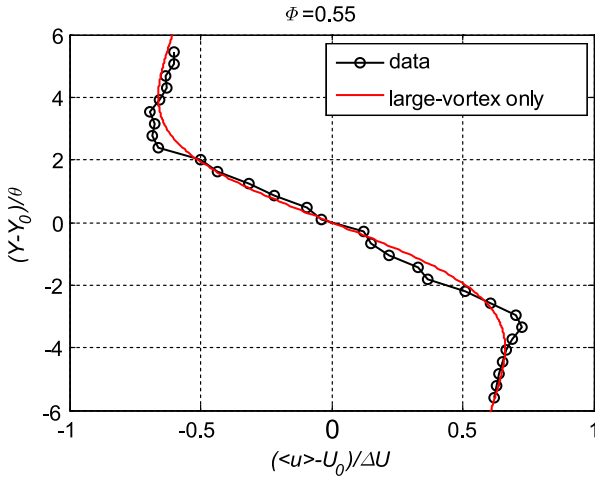
Fig. A1 Comparison between the computed and the measured velocity profiles at the phase when the LV passes through the measurement location. Model calculation is based on using only the first two terms on the right-hand side of Eq. (4). Model parameters are $\Gamma_{o,v}/\Delta U\theta = 17.45$, $R_{o,v}/\theta = 3.17$, and $L_x/\lambda = N = 50$.
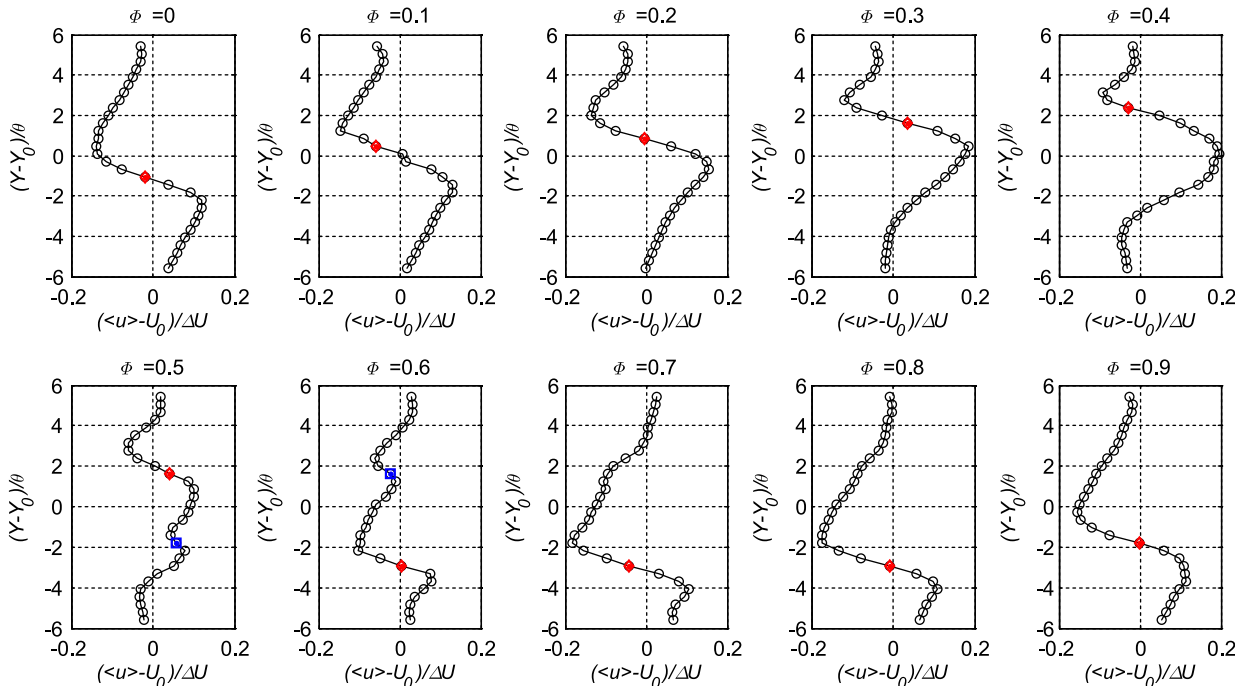
Fig. A2   Profiles of the residual streamwise velocity at different phases of the oscillation cycle. Model parameters are $\Gamma_{o,v}/\Delta U\theta = 17.45$, $R_{o,v}/\theta = 3.17$, and $L_x/\lambda = N = 50$. Diamonds mark the location of highest magnitude of negative shear, and squares identify second local maxima in the magnitude of the negative shear.
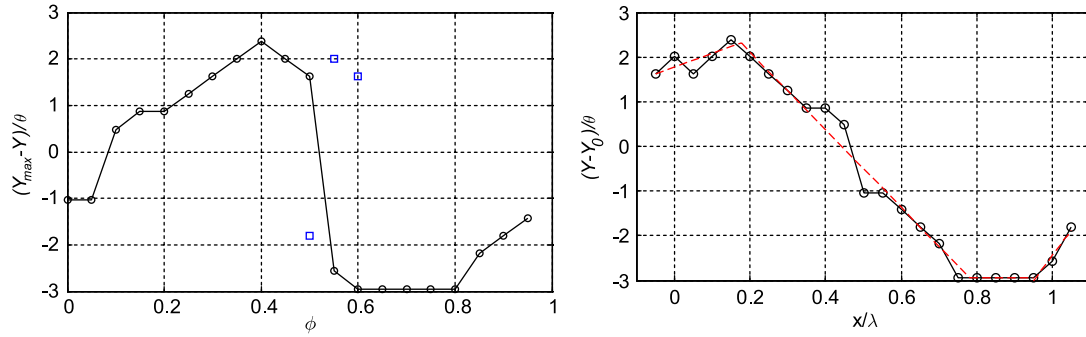
Fig. 15   Left plot: measured _Y_ location of the maximum shear (circles) versus phase of the oscillation cycle. The squares represent the _Y_ location of a second local maximum in the magnitude of the negative shear. Right plot: locus of the VS in a given wavelength of the vortex-array model. Circles show the locus based on experimental data.

location from the top to the bottom of the LV. The squares in Fig. 15 (left) represent the _Y_ locations of the second local shear maximum identified in Fig. A2 at phases around $\Phi = 0.55$. Indeed, the large-scale vortex depicted on the right side of the flow visualization image in Fig. 4 shows that the two ends of the vortex sheet may co-exist simultaneously at the top and bottom of the vortex structure.

In the model, the _Y_ location of the centers of the small-scale vortices representing the VS is set following the _Y_ location of the maximum shear (Y_{max}) at different phases of the oscillation cycle. For the purposes of the model, the Y_{max} variation with phase for the braid is converted into variation with _X_ to describe the locus along which the _n_ small-scale vortices are placed. This is achieved by multiplying the time corresponding to a given phase by U_o (the convection velocity used in the model). The resulting locus of the VS is shown in Fig. 15 (right) by circles, after shifting the phase such that the center of the LV is located at $X = 0$ (and λ). To simplify the VS representation and to address some of the scatter observed in the experimentally determined sheet locus, piecewise linear representation is employed, resulting in four different linear segments, as depicted with the broken line in Fig. 2 (right). Other representations of the sheet locus data (e.g., polynomial fit) are possible but the piecewise linear representation is selected here for simplicity. Within each segment containing more than two points, a least-squares line fit to the data is employed to define the line representing the vortex sheet locus. It should be noted that, in the model, the small vortices representing the vortex sheet are distributed equally spaced (in _X_) along the locus shown in Fig. 15 (right) over the domain $X/\lambda = -0.05$ to 1.05. The model also contains the parameter dY_c, which allows imposition of a _Y_ offset between the core center of the large vortex and Y_o.

In step 3, the values for model parameters $\Gamma_{o,vs}$, $\Gamma_{o,v}$, $R_{o,vs}$, $R_{o,v}$, and dY_c are found using a steepest-descend optimization routine to minimize the sum of the squared error between the model calculation and the measurements of $\langle u \rangle$ at all _Y_ locations and phases of the oscillation cycle, as given by

$$\varepsilon_{Y,\Phi}^2 = \sum_\Phi \sum_y \left[\langle u(Y,\Phi) \rangle_c - \langle u(Y,\Phi) \rangle_m \right]^2 \quad (A2)$$

For simplicity, the optimization was carried out for one parameter at a time. A more sophisticated method of optimization may lead to improvements in the model results. No such method was pursued, given that the implemented approach was sufficiently satisfactory in capturing the key features of the measured data.

Acknowledgments

References

[1] Perry, A. E., and Chong, M. S., "On the Mechanism of Wall Turbulence," _Journal of Fluid Mechanics_, Vol. 119, June 1982, pp. 173–217.
doi:10.1017/S0022112082001311
[2] Perry, A. E., Henbest, S., and Chong, M. S., "A Theoretical and Experimental Study of Wall Turbulence," _Journal of Fluid Mechanics_, Vol. 165, April 1986, pp. 163–199.
doi:10.1017/S0022112086000304X
[3] Ahn, B.–K., Graham, W. R., and Rizzi, A., "A Structure-Based Model for Turbulent-Boundary-Layer Wall Pressures," _Journal of Fluid Mechanics_, Vol. 650, May 2010, pp.443–478.
doi:10.1017/S0022112009993727
[4] Acton, E., "A Modelling of Large Eddies in an Axisymmetric Jet," _Journal of Fluid Mechanics_, Vol. 98, No. 1, 1980, pp. 1–31.
doi:10.1017/S0022112080000018
[5] Kitaplioglu, C., and Kibens, V., "Discrete Vortex Modeling of an Axisymmetric Jet Flowfield," AIAA Paper 1980-1003, 1980.
[6] Naguib, A. M., Vitek, J., and Koochesfahani, M. M., "Finite-Core Vortex Array Model of the Wake of a Periodically Pitching Airfoil," _AIAA Journal_, Vol. 49, No. 7, 2011, pp. 1542–1550.
doi:10.2514/1.J050881
[7] Leonard, A., "Vortex Methods for Flow Simulation," _Journal of Computational Physics_, Vol. 37, No. 3, 1980, pp. 289–335.
doi:10.1016/0021-9991(80)90040-6
[8] Koochesfahani, M. M., and Dimotakis, P. E., "Effects of a Downstream Disturbance on the Structure of a Turbulent Plane Mixing Layer," _AIAA Journal_, Vol. 27, No. 2, 1989, pp. 161–166.
doi:10.2514/3.10078
[9] Monnier, B., Naguib, A. M., and Koochesfahani, M. M., "Influence of Structural Flexibility on the Wake Vortex Pattern of Airfoils Undergoing Harmonic Pitch Oscillation," _Experiments in Fluids_, Vol. 56, April 2015, p. 80.
doi:10.1007/s00348-015-1946-2
[10] Dewey, P. A., Quinn, D. B., Boschitsch, B. M., and Smits, A. J., "Propulsive Performance of Unsteady Tandem Hydrofoils in a Side-by-Side Configuration," _Physics of Fluids_, Vol. 26, No. 4, 2014, Paper 041903.
doi:10.1063/1.4871024
[11] Boschitsch, B. M., Dewey, P. A., and Smits, A. J., "Propulsive Performance of Unsteady Tandem Hydrofoils in an In-Line Configuration," _Physics of Fluids_, Vol. 26, No. 5, 2014, Paper 051901.
doi:10.1063/1.4872308
[12] Cimbala, J. M., Naguib, H. M., and Roshko, A., "Large Structure in the Far Wakes of Two-Dimensional Bluff Bodies," _Journal of Fluid Mechanics_, Vol. 190, May 1988, pp. 265–298.
doi:10.1017/S0022112088001314
[13] Lim, T. T., _Flow Visualization Techniques and Examples_, 2nd ed., edited by A. J. Smits, and T. T. Lim, Imperial College Press, London, 2012, pp. 66–69.
doi:10.1142/p808
[14] Koochesfahani, M. M., Catherasoo, C. J., Dimotakis, P. E., Gharib, M., and Lang, D. B., "Two-Point LDV Measurements in a Plane Mixing Layer," _AIAA Journal_, Vol. 17, No. 12, 1979, pp. 1347–1351.
doi:10.2514/3.7632

I. Gursul
Associate Editor